

1 Measuring single cell divisions in 2 human tissues from multi-region 3 sequencing data

4 Benjamin Werner^{1,2,*}, Jack Case^{1,3}, Marc J. Williams^{4,5,6}, Kate Chkhaidze¹, Daniel
5 Temko⁴, Javier Fernandez-Mateos¹, George D. Cresswell¹, Daniel Nichol¹, William
6 Cross⁴, Inmaculada Spiteri¹, Weini Huang^{7,8}, Ian Tomlinson⁹, Chris P. Barnes^{5,10},
7 Trevor A. Graham^{4,*} & Andrea Sottoriva^{1,*}
8

9 ¹Evolutionary Genomics & Modelling Lab, Centre for Evolution and Cancer, The Institute of Cancer
10 Research, Sutton, London SM2 5NG, UK

11 ²Evolutionary Dynamics Group, Centre for Cancer Genomics & Computational Biology, Barts Cancer
12 Institute, Queen Mary University of London, Charterhouse Square, London, UK EC1M 6BQ.

13 ³University of Cambridge

14 ⁴Evolution and Cancer Laboratory, Centre for Cancer Genomics & Computational Biology, Barts Cancer
15 Institute, Queen Mary University London, London, Charterhouse Square, London, UK EC1M 6BQ.

16 ⁵Department of Cell and Developmental Biology, University College London, London, UK

17 ⁶Centre for Mathematics and Physics in the Life Sciences and Experimental Biology (CoMPLEX),
18 University College London, London, UK

19 ⁷Group of Theoretical Biology, The State Key Laboratory of Biocontrol, School of Life Science,
20 Sun Yat-sen University, Guangzhou, 510060 China

21 ⁸School of Mathematical Sciences, Queen Mary University London, London, UK.

22 ⁹Institute of Cancer and Genomic Sciences, University of Birmingham, Birmingham, UK

23 ¹⁰UCL Genetics Institute, University College London, London, UK

24

25 *Correspondence should be addressed to: b.werner@qmul.ac.uk, t.graham@qmul.ac.uk,
26 andrea.sottoriva@icr.ac.uk

27

28

29

30 **Abstract**

31 Both normal tissue development and cancer growth are driven by a branching
32 process of cell division and mutation accumulation that leads to intra-tissue
33 genetic heterogeneity. However, quantifying somatic evolution in humans
34 remains challenging. Here, we show that multi-sample genomic data from a
35 single time point of normal and cancer tissues contains information on single-cell
36 divisions. We present a new theoretical framework that, applied to whole-
37 genome sequencing data of healthy tissue and cancer, allows inferring the
38 mutation rate and the cell survival/death rate per division. On average, we found
39 that cells accumulate 1.14 mutations per cell division in healthy haematopoiesis
40 and 1.37 mutations per division in brain development. In both tissues, cell
41 survival was maximal during early development. Analysis of 131 biopsies from
42 16 tumours showed 4 to 100 times increased mutation rates compared to
43 healthy development and substantial inter-patient variation of cell
44 survival/death rates.

45

46 **Introduction**

47 Most cells in human tissues have a limited life span and need to be replenished
48 for tissues to remain functional¹⁻³. This cell turnover leads to somatic evolution,
49 with cells accumulating mutations upon which selection may act^{4,5}. Inter- and
50 intra-tumour genetic heterogeneity^{6,7} as well as treatment resistance^{8,9} are now
51 understood to be consequences of somatic evolutionary processes. Recent
52 studies demonstrate somatic evolution in healthy non-cancerous tissues

53 throughout life¹⁰⁻¹⁴. Normal brain cells carry hundreds of mutations weeks after
54 conception¹² and normal skin or esophagus cells accumulate hundreds of cancer
55 driver mutations during adulthood^{10,11}.

56 These observations call for a better quantitative understanding of the somatic
57 evolutionary forces in both cancerous and healthy tissues¹⁵. However, unlike
58 species evolution for which a timed fossil record exists^{16,17}, the lack of sequential
59 human data over time due to ethical and technical limitations is a major obstacle.
60 Furthermore, some evolutionary forces are difficult to measure even having the
61 data. For example, the mutational burden in a tissue is the combined effect of
62 per-cell mutation and per-cell survival rates, which remain hidden in sequencing
63 data^{18,19} (Figure 1). Currently, we cannot independently infer these two for
64 somatic evolution fundamental quantities from single time point sequencing
65 data.

66 Here, we show that multiple bulk or single cell sequencing from the same patient
67 contain recoverable information on these important quantities that can be
68 recovered with evolutionary theory. This allows inferring *in vivo* cell mutation
69 and cell survival rates in tissues of individual humans from single time point
70 sequencing data.

71

72 We draw our inferences by defining and quantifying the distribution of
73 mutational distances amongst multiple samples. We first discuss the required
74 theoretical considerations and derive an analytical expression for the expected
75 distribution of mutational distances from multi-sample sequencing data. We
76 introduce a Bayesian sampling framework based on the mutational distance

77 distribution, allowing us to disentangle mutation rates per cell division and cell
78 survival/death rates. We apply this framework to whole genome single cell
79 sequencing data of haematopoiesis and brain tissue and measure both
80 evolutionary parameters during early development. Finally, we utilize multi-
81 sample sequencing data on 16 tumours to infer patient specific evolutionary
82 parameters in human cancers.

83 **Results**

84 **The distribution of mutational distances**

85 All cells in a human tissue must have descended from a most recent common
86 ancestor cell (MRCA) that existed briefly during early development. Similarly, all
87 cells in a sample of a tissue must have descended from a (different) MRCA that
88 was present in that tissue at an earlier time (Figure 1a). Mutations found in all
89 cells of the sample (clonal mutations) were present in this MRCA. If we take
90 multiple samples of the same tissue, we can reconstruct the mutational profile
91 (all mutations carried by a single cell) of multiple ancestral cells (Figure 1a).
92 Typically, these ancestral cells differ in their exact mutational profile between
93 one another, because mutations inevitably accumulate differently in distinct
94 lineages (Figure 1b). We use the differences of the mutational profiles between
95 ancestral cells to construct the distribution of mutational distances. We define a
96 mutational distance as the number of mutations different between any two
97 ancestral cells (Figure 1c). In the language of set theory, if ancestral cell 1 carries
98 a set of mutations A and ancestral cell 2 carries a set of mutations B , then by
99 definition, both cells must have coalesced from an earlier ancestral cell (Figure

100 1a). The mutational profile of this cell is given by the intersection $A \cap B$. This
101 allows us to construct two mutational distances given by

102

$$103 \quad y_1 = |A \setminus (A \cap B)| \quad \text{and} \quad y_2 = |B \setminus (A \cap B)|. \quad (1)$$

104

105 This process can be iterated for increasing combinations of samples per tumour.

106 We now turn to quantitative expressions for the expected distribution of

107 mutational distances $P(y)$. In a single division, the probability of a cell to acquire

108 X novel mutations follows a *Poisson* distribution

109

$$110 \quad P(X) = \frac{(\mu L)^X}{X!} e^{-\mu L}. \quad (2)$$

111

112 Here, μ is the mutation rate (in units of base pairs per cell division) and L the size

113 of the sequenced genome. Throughout the manuscript, we assume a constant

114 mutation rate and do not consider more punctuated catastrophic events or

115 mutational bursts. Distances between cells of a lineage may arise from more than

116 a single cell division. Instead, double, triple and higher modes of cell division

117 contribute to the distribution of mutational distances of multi-sample samples.

118 In general, a cell accumulates $X_1 + X_2 + \dots + X_n$ number of novel mutations after

119 n divisions, which is again *Poisson* distributed.

120

121 In addition, we must account for cell death or differentiation, leading to lineage

122 loss. We therefore introduce a probability β of having two surviving lineages

123 after a cell division and a probability $1 - \beta$ of a single surviving lineage (cell

124 death). We can split the total of n cell divisions into r divisions that result in two

125 surviving lineages (branching divisions) and m divisions with only a single
126 surviving lineage (non-branching divisions). The number of non-branching
127 events m is again a random variable, which follows a *Negative Binomial*
128 distribution

129

$$130 \quad P(m|r) = \binom{r+m-1}{r-1} \beta^r (1-\beta)^m. \quad (3)$$

131

132 The number of mutations acquired between two branching divisions depends
133 jointly on the *Poisson* distributed number of mutations and the *Negative binomial*
134 distributed number of non-branching divisions m . Formally, we can write for the
135 total number of mutations between two branching divisions

136

$$137 \quad Y = \sum_{i=1}^m X_i. \quad (4)$$

138

139 Equation (4) is a random sum of random variables and different combinations of
140 X and m imply the same mutational burden Y within a single cell lineage.
141 Intuitively, a measured mutational burden in a single lineage can result from
142 either many non-branching divisions with a low mutation rate or, alternatively a
143 few non-branching divisions with high mutation rate. The mutational burden of a
144 single sample is insufficient to disentangle per-cell mutation and per-cell
145 survival/death rates.

146

147 We therefore turn to the number of mutations different between ancestral cells.

148 Suppose two ancestral cells are separated by r branching divisions. Following

149 from equation (4), we can calculate the probability distribution of the number of
 150 acquired mutations $P(y|r)$ after r branching divisions

151

$$152 \quad P(y|r) = \sum_{i=r}^{\infty} \binom{i-1}{r-1} \beta^r (1-\beta)^{i-r} e^{-i\mu L} \frac{(i\mu L)^y}{y!}. \quad (5)$$

153

154 Here the sum starts at r , as we need to have at least r branching divisions and
 155 runs to infinity as in principal infinitely many non-branching divisions can occur
 156 (with vanishingly low probability). Finally, we need the expected distribution of
 157 branching divisions $P(r)$ in a growing population of cells, which follow from
 158 coalescence theory²⁰⁻²². For a growing population, e.g. human tissues during
 159 early development or cancer growth, we find

160

$$161 \quad P(r) = \frac{\exp\left(-\frac{e^{-\beta(r+1)}}{\beta}\right) - \exp\left(-\frac{e^{-\beta r}}{\beta}\right)}{1 - \exp\left(-\frac{e^{-\beta}}{\beta}\right)}. \quad (6)$$

162

163 We provide a more detailed derivation in the Methods. Combining equations (5)
 164 and (6) we arrive at the final expression for the expected distribution of
 165 mutational distances in an exponentially growing population

166

$$167 \quad P(y) = \sum_{r=1}^{\infty} \sum_{i=r}^{\infty} P(r) \binom{i-1}{r-1} \beta^r (1-\beta)^{i-r} e^{-i\mu L} \frac{(i\mu L)^y}{y!}. \quad (7)$$

168

169 The two evolutionary parameters of interest here, the mutation rate per cell
 170 division μ and the cell survival rate β , disentangle in equation (7). There are
 171 approximately four possible regimes for the distribution of mutational distances,

172 discriminated by uni- or multimodality determined by combinations of small or
173 large μ and β . In Figure 2a we show four representative realisations of equation
174 (7). The distribution of mutational distance is unimodal for sufficiently small
175 mutation rate μ (bottom panels in Figure 2a) with a single peak at the mean
176 mutational distance μL . The per-cell survival probability β determines the
177 weight of the distribution towards larger distances. For $\beta = 1$ the distribution is
178 sharply located around the mean mutation rate. However, for smaller β more
179 weight is given to larger distances and the distribution gets a fat tail. The same is
180 true for the case of high mutation rate μ , except the distribution is multi-modal
181 with peaks separated by multiples of the mean mutational distance μL (Figure
182 2a). Again, β determines the weight to higher mutational distances with lower β
183 causing a distribution with a long oscillating tail (top right panel in Figure 2a).
184 Note, the y-axes in Figure 2a correspond to the probabilities of observing certain
185 mutational distances. Lower probabilities require a higher resolution and
186 therefore more sampling to resolve the exact shape of the distribution. In
187 practice, the distribution of mutational distances is easiest to recover from data
188 with low μ and high β (fewest number of tissue samples required), whereas most
189 samples are required for high μ and low β (top right panel in Figure 2a).

190

191 **Computational validation and MCMC inference framework**

192 We implemented stochastic spatial simulations of mutation accumulation in
193 growing tissues using previously published code²³. Briefly, cell birth and death
194 on a 2- or 3-dimensional grid was simulated using a Gillespie algorithm²⁴. During
195 division, cells accumulate a number of new mutations drawn from a *Poisson*
196 distribution. Simulations were stopped when the tissue reached ~ 1 million cells.

197 This allowed us to take samples (either single cells or bulks) and construct all
198 pairwise mutational distances of all ancestral cell lineages detectable in the
199 samples. In Figure 2b we show an example of the mutational distance
200 distribution derived from 200 samples of a stochastic simulation (dots)
201 compared to the theoretical prediction (dashed line).

202 We want to infer the microscopic evolutionary parameters μ and β given a
203 measured distribution of mutational distances. This can be done by Markov
204 chain Monte Carlo methods (MCMC). We implemented a standard Metropolis-
205 Hastings algorithm. In brief, a random pair of parameters μ and β is drawn from
206 uninformed uniform distributions and the likelihood of the model parameters
207 given the data is calculated. The new set of parameters is accepted with a
208 probability proportional to the likelihood ratio of the new and old parameter set
209 (see Methods for more details). This framework recovers the true underlying
210 parameters from stochastic simulations (Figure 2c & Supplementary Figures 17
211 to 21).

212

213 ***In vivo* mutation and cell survival rate inference in healthy** 214 **haematopoiesis during early development**

215 We discuss the *in vivo* mutation accumulation in healthy haematopoiesis during
216 early development as a first application. The cell population is growing and we
217 expect a low mutation rate and a high per-cell survival rate during the
218 development of early haematopoiesis^{13,25}. In a recent study, Lee-Six and
219 colleagues¹³ sequenced the genome of 89 healthy haematopoietic stem cells of a
220 single 59-year-old male and subsequently constructed the phylogeny of healthy

221 haematopoiesis. They estimated the per-cell mutation rate to be 1.2 mutations
222 per genome per division during early development assuming perfect cell
223 doublings. Using the same data we construct the pairwise mutational distances
224 of all ancestral cells limited to the 20 earliest branching events. The resulting
225 distribution of mutational distances is shown in Figure 3a. We then use the same
226 MCMC framework discussed above to jointly infer the mutation and cell survival
227 rate. The MCMC algorithm rapidly converges to a fixed set of parameters (
228 Supplementary Figure 17). In Figure 3a and 3b we show the posterior parameter
229 distributions after an initial burn in phase of 200 MCMC steps. In agreement with
230 Lee-Six and colleagues, we find a mutation rate of $\mu = 1.14_{-0.24}^{+0.12}$ mutations per
231 genome per division (shown is the medium mutation rate per bp/cell-division
232 and 95% credibility intervals inferred from the MCMC posterior parameter
233 distribution), which corresponds to a mutation rate of $\mu = 3.9 \times 10^{-10}$ base
234 pairs/division (assuming 3×10^9 bp in the human genome). Furthermore, we
235 infer a per-cell survival rate of $\beta = 0.96_{-0.102}^{+0.038}$, independently confirming the
236 original assumption of almost perfect cell doubling during early development¹³.

237

238 ***In vivo* mutation and cell survival rate inference in single neurons**

239 **during development**

240 In a recent publication, Bae and colleagues¹² collected single neurons from 3
241 fetuses 15 to 21 weeks post conception. Cells were expanded in culture and the
242 whole genome was sequenced. Here we focus on the case where 14 whole
243 genome sequenced single neurons were available (1 fetus 17w4d after
244 conception). Again, we inferred all pairwise mutational differences, constructed

245 the corresponding distribution of mutational distances (Figure 4a) and used our
246 MCMC framework for joint parameter estimates. The MCMC converges rapidly
247 and we find sharply localised posterior distributions for the mutation and cell
248 survival rate. We infer a median mutation rate of $\mu = 1.37_{-0.1}^{+0.1}$ mutations per
249 genome per division (corresponding to a mutation rate of $\mu = 4.6 \times 10^{-10}$ base
250 pair/division) and a per-cell survival rate of $\beta = 0.998_{-0.01}^{+0.002}$. This inference
251 agrees with Bae and colleagues original estimate of 1.3 mutations per genome
252 per division based on a weighted average of all 3 fetuses, again assuming no cell
253 death during early development. It also agrees with estimates of 1.2 mutations
254 per division from de novo SNVs in familial trios²⁶. The almost identical mutation
255 rates in haematopoietic and brain tissue during early development may not be
256 surprising. We would expect the DNA duplication and repair machinery to be
257 stable across tissues during early development. It may even remain stable
258 throughout life, as suggested by the linear rate of mutation accumulation with
259 age across individuals²⁷⁻²⁹.

260

261 ***In vivo* mutation and cell survival rates in human tumours**

262

263 We then investigated the per-cell mutation and survival rates in individual
264 tumours. We analysed whole genome or exome sequencing of 131 biopsies from
265 16 tumours comprised of 1 colon adenoma, 7 colon carcinomas, 5 clear cell renal
266 carcinomas and 2 lung squamous cell carcinomas (Table 1). When whole genome
267 sequencing was available, the mutational load was sufficient to apply the
268 inference framework to each chromosome separately (Figure 5 and
269 Supplementary Figures 1-9). The analysis was restricted to regions of

270 chromosomes with same copy number profile in all samples of a tumour and
271 inferences were normalised by copy-number and genome content. The
272 resolution to infer the distribution of mutational distances from tumours was
273 lower compared to healthy haematopoiesis or brain during development.
274 Nevertheless, in most cases, the reconstructed distributions recover important
275 features of the theoretical distribution (Supplementary Figures 1-9 and 14). We
276 found that mutation rates per cell division were 4 to 100 times higher in tumours
277 compared to healthy tissue, ranging from 2.91×10^{-9} (bp/division) in the colon
278 adenoma to 53×10^{-9} (bp/division) in one lung squamous cell carcinoma (Table
279 1). Mutation rates differ significantly between patients but not across
280 chromosomes of the same patient (Supplementary Figures 11 and 12). Overall
281 this suggests important differences in mutation accumulation at the single cell
282 level between tumours and is in agreement with recent experimental *in vitro*
283 single cell mutation rate inferences^{29,30}.

284

285 To further unravel the underlying differences in mutation accumulation during
286 tumour growth, we decomposed somatic mutations into the most prevalent
287 trinucleotide mutational signatures³¹ for three whole-genome sequenced
288 colorectal carcinomas and inferred per-cell mutation and per-cell survival rates
289 per signature in each chromosome (Figure 5). Again, we find significant
290 differences between patients (Supplementary Figure 13), further supporting
291 inter-tumour differences of mutation accumulation at the single cell level.

292

293 The inter-patient variation of the cell survival rate was evident. Whereas in
294 healthy tissue almost all cells survive during development, in tumours cell

295 survival rates vary between 0.34 in one MSI+ colon carcinoma up to 0.86 in one
296 renal cell carcinoma (Table 1). Again, per-cell survival rates were overall
297 consistent if inferred from chromosomes of individuals, but varied significantly
298 between patients (Figure 6 and Supplementary Figure 12). The underlying
299 reasons for this inter-patient variation may be cell intrinsic and/or extrinsic, e.g.
300 high cell death due to genomic instability, high mutational burden or immune
301 surveillance. It will be of high interest to further unravel these differences on a
302 patient specific basis in future studies. It should be noted that the inferred cell
303 survival rates are high compared to previous estimates^{32,33}. This is a direct
304 consequence of the joint inference of mutation and cell survival rates that was
305 not possible in earlier work.

306

307 **Discussion**

308 Here we presented a framework that allows disentangling the microscopic
309 evolutionary forces of mutation and survival rates per cell division in humans
310 from single time point measurements. Leveraging data on mutations in healthy
311 haematopoiesis¹³ and brain tissue¹², we found, in agreement with previous
312 estimates, mutation rates of 1.14 and 1.37 mutations per whole genome per cell
313 division. Mutation rates were 4 to 100 times higher in cancers and showed
314 considerable inter-patient variation.

315

316 The inference framework presented here relies on some assumptions. Mutation
317 and cell survival rates are kept constant through time and spatial location. We do
318 not consider significant changes in cell fitness during growth and/or spatial

319 resource constraints. These limitations are more important for tumour specific
320 inferences and less relevant for healthy tissue. The exact temporal and spatial
321 change of the underlying microscopic evolutionary parameters over the lifetime
322 of an individual tumour remains an open question. In some cases, there is
323 evidence for singular catastrophic events³⁴ and mutational signatures may
324 change between resection and relapse³⁵. However, it will also be important to
325 disentangle mutation and cell population dynamic processes in these cases. A
326 more fine-grained sampling over space and time is needed to better access if and
327 how evolutionary parameters change within tumours. Given the technological
328 advances in single cell genomics^{36,37}, sequencing of potentially thousands of
329 single cells would lead to significant information gain. This will allow probing
330 potential changes of these evolutionary parameters over time.

331

332 Furthermore, we expect the inter-patient variation of per-cell mutation and
333 survival rates to directly influence clinically important variables, such as the
334 likelihood of pre-existing treatment resistance³⁸, tumour age and
335 aggressiveness³⁹. Measuring microscopic evolutionary forces in humans allows
336 for a mechanistic foundation for precision medicine.

337

338

339

340

341

342

343 **Methods**

344

345 **Branching distribution in exponentially growing populations**

346 To calculate the expected distribution of branching events in an exponentially
347 growing population, we can make use of coalescence theory^{20,21}. Note that in
348 coalescence theory one usually uses a backward time convention. If a population
349 grows exponentially with $N(\tau) = e^{\beta\tau}$, coalescence considers backward time
350 $t = -\tau$ such that populations effectively shrink exponentially. The probability of
351 coalescence $P_{\zeta}(t)$ at time t in an exponentially growing population is given by

352

$$353 \quad P_{\zeta}(t) = \frac{1}{N(t)} \prod_{s=0}^{t-1} \left[1 - \frac{1}{N(s)}\right] \approx \frac{e^{\beta t}}{N_0} \exp\left(\frac{1-e^{\beta t}}{\beta N_0}\right), \quad (8)$$

354

355 where $N(t)$ is the size of the growing population at time t . In our case, we are
356 concerned with mutational distances and thus we ask for the distribution of
357 times between coalescence events Δt rather than the distribution of coalescence
358 times t . However, we can directly infer this distribution from equation (8), by
359 rewriting $\Delta t = t_0 - t$ as the time of the initiating cell population at some point in
360 the past. By substituting $t_0 = \log(N_0)/(\beta)$, we have $\Delta t = \frac{\log(N_0)}{\beta} - t$ and we find

361 for the distribution of times between coalescence events

362

$$363 \quad P(\Delta t) = P\left(\frac{\log(N_0)}{\beta} - t\right) = e^{-\beta\Delta t} \exp\left(\frac{1-N_0 e^{-\beta\Delta t}}{\beta N_0}\right). \quad (9)$$

364

365 This is for large N_0 well approximated by

366

367
$$P(\Delta t) = e^{-\beta \Delta t} \exp\left(-\frac{e^{-\beta \Delta t}}{\beta}\right). \quad (10)$$

368

369 We show the validity of this approximation in Supplementary Figure 16. The
370 normalized expression holds for all $N_0 \geq 1$. We can discretise this probability
371 density function to derive at the probability for the number of branching
372 divisions r via

373

$$\begin{aligned} P(r) &= \int_r^{r+1} d(\Delta t) P(\Delta t) = \int_r^{r+1} d(\Delta t) e^{-\beta \Delta t} \exp\left(-\frac{e^{-\beta \Delta t}}{\beta}\right) \\ &= \exp\left(-\frac{e^{-\beta(r+1)}}{\beta}\right) - \exp\left(-\frac{e^{-\beta r}}{\beta}\right). \end{aligned} \quad (11)$$

375

376 As we are interested in positive branch length only, we need to normalise the
377 distribution for non-negative integers such that $1 = \frac{1}{C} \sum_{i=1}^{\infty} P(r = i)$. The
378 normalising factor is $C = 1 - \exp\left(-\frac{e^{-\beta}}{\beta}\right)$, and the distribution of branching
379 divisions r in an exponentially expanding cell population becomes

380

381
$$P(r) = \frac{\exp\left(-\frac{e^{-\beta(r+1)}}{\beta}\right) - \exp\left(-\frac{e^{-\beta r}}{\beta}\right)}{1 - \exp\left(-\frac{e^{-\beta}}{\beta}\right)}. \quad (12)$$

382

383 Equation (12) together with equation (6) in the main text allows a complete
384 description of the expected distribution of mutational distances in exponentially
385 growing populations. It has to be noted that the coalescence approximation used

386 here is based on a deterministic exponential growth function. It is known that
387 such approaches do not always fully capture the full stochasticity especially at
388 small population sizes and birth-death processes often perform better²². The
389 individual based computer simulations used here are implementations of the
390 Gillespie algorithm and are exact numerical representations of the underlying
391 stochastic process. However, a further analysis on the stochasticity of the
392 process for small population sizes is warranted.

393

394 **Interpretation of effective survival rate**

395

396 Throughout the manuscript we use the concept of the effective cell survival rate
397 β . One can also formulate cell death with a microscopic perspective given a
398 probability α for a daughter cell to die (or differentiate) after division. Such a
399 probability allows for three outcomes after a cell division: with probability
400 $(1 - \alpha)^2$ both daughter cells survive, with probability $2\alpha(1 - \alpha)$ one daughter
401 cell survives and with probability α^2 both daughter cells die. However, as we are
402 bound to find surviving cell lineages in every possible measure of tumours, none
403 of the observed cell lineages can have gone extinct. Mathematically, this implies
404 that measurement conditions cell division on non-extinction of both daughter
405 cells and we can write

406

$$407 \quad \beta \equiv P(\text{successful division} | \text{non extinction}) = \frac{P(\text{successful division \& non extinction})}{P(\text{non extinction})}.$$

408

409 With the corresponding probabilities α we get

410

411
$$\beta = \frac{(1-\alpha)^2}{1-\alpha^2} = \frac{1-\alpha}{1+\alpha}. \quad (13)$$

412

413 We also can rearrange equation (13) to solve for α ,

414

415
$$\alpha = \frac{1-\beta}{1+\beta}. \quad (14)$$

416

417 If we interpret α as the probability of random cell death after a division, α must
418 be smaller than 1/2. If α were larger than 1/2, tumour populations extinct
419 almost surely after sufficiently many cell divisions. This implies $\beta > 1/3$ for
420 growing populations.

421

422 **Simulations of mutation accumulation in growing tissues**

423 We simulated cell populations of ~ 1 million cells on a grid with varying birth
424 death and mutation rates using an implementation of the Gillespie algorithm
425 based on code published in²³. The code is available at
426 <https://github.com/sottorivalab/CHES.cpp>. A cell division produces two
427 surviving cells with probability β or one surviving cell with probability $1 - \beta$.
428 During each division, each daughter cell inherits the mutations of its parent and
429 in addition accumulates novel mutations. The number of novel mutations is
430 drawn from a *Poisson* distribution with mean μ . During simulations, the
431 mutations for each cell as well as the division history of each cell are recorded.

432

433 We took samples (between 1 and 10k cells per sample) from each simulated
434 tumour. For most inferences, we used maximal distance sampling. Sequencing
435 errors were simulated for each bulk by binomial sampling assuming sequencing
436 depths of 100x, by generating dispersed coverage values for input mutations. We
437 do that by sampling a coverage from a Poisson distribution: $\text{Poisson}(\lambda = Z)$ with
438 mean λ equal to a desired sequencing depth Z . Once we have sampled a depth
439 value k for a mutation, we sample its frequency (number of reads with the
440 variant allele frequency) with a Binomial trial. We use $f \sim \text{Binomial}(n, k)$, where
441 n is the proportion of cells carrying this mutation given all cells sampled in the
442 simulated biopsy. This generates realistic mutation distributions comparable to
443 available genomic sequencing data.

444

445 **Bayesian parameter inference**

446 We use a Markov chain Monte Carlo method (MCMC) to recover the mutational
447 distance μL and the cell survival rate β given a measured distribution of
448 mutational distances. More precisely we implemented a standard Metropolis-
449 Hastings-algorithm following below steps:

- 450 (i) Create a new random set of model parameters \mathbf{w} given the current set
451 of parameters \mathbf{v} from a defined probability density Q , such that
452 $Q(x|y) = Q(y|x)$.
- 453 (ii) Calculate the likelihood $L(P(\mathbf{w}))$ of the model distribution $P(\mathbf{w})$ given
454 the data.
- 455 (iii) Calculate the ratio of the new and old likelihood $\rho = L(P(\mathbf{w}))/$
456 $L(P(\mathbf{v}))$. Accept the new parameter set with probability ρ otherwise
457 reject.

458 (iv) Repeat

459 In our case the model distribution is given by equation (7) in the main text. To
460 calculate the likelihood of equation (7) given the data, we have to choose a cut off
461 for the infinite sums. However, real data always has a maximum mutational
462 distance. Higher terms of the infinite sums contribute to higher mutational
463 distances. The distribution of interest does not change for a sufficiently high cut
464 off and each observed data set only requires finite many terms. Here we used
465 $r = i = 30$ as upper cut-off, which is a conservative choice. We used uninformed
466 uniform prior distributions for mutational distance μL and the per-cell survival
467 rate β in all cases. Point estimates were extracted as sample medians from the
468 MCMC inferences. The ranges of the uniform priors were adjusted to optimise
469 acceptance rates and computational time. In our implementation, a new set of
470 parameters is relative to the previously accepted parameter set $\mathbf{w}_{New} = \mathbf{w}_{Old} +$
471 $\Phi(\mathbf{w})$, where Φ is the prior parameter distribution. A typical range used in our
472 inference scheme is $\Phi_{\text{uniform}}(\beta) = [-0.06, +0.06]$ and $\Phi_{\text{uniform}}(\mu) =$
473 $[-0.15, +0.15]$. We also tested *Gamma* prior distributions and did not see
474 differences in convergence. One numerical realisation of the Log-Likelihood
475 function is shown in Supplementary Figure 18 and example traces of the MCMC
476 algorithm are shown in Supplementary Figure 17. We also tested the influence of
477 sequencing depth and spatial sampling strategies on the performance of the
478 MCMC inference framework (Supplementary Figures 19 & 20). The code for the
479 MCMC inference is available at [https://github.com/sottorivalab/MCMC-](https://github.com/sottorivalab/MCMC-MutationalDistances)
480 [MutationalDistances](https://github.com/sottorivalab/MCMC-MutationalDistances).

481

482 **Mutational signature analysis**

483 For each sample we found the set of signatures (among those signatures
484 reported in CRC) that best explained the totality of mutations in the sample. We
485 did a non-negative regression of the sample's mutations against all the CRC
486 signatures⁴⁴ and found those signatures with non-zero coefficients. We took
487 these as the candidate signatures for each sample.

488

489 For each mutation in each sample, we determined the likelihood of the mutation
490 under each of the candidate signatures. We assigned a mutation to a candidate
491 signature where the likelihood under that signature was at least twice that under
492 any other. If there was no such signature, we assigned the mutation to "Other".
493 The method was originally developed in⁴⁴ and is based on the R-package
494 "SomaticSignatures"⁴⁵. We did not adjust for differences in nucleotide
495 composition when calculating differences between coding and non-coding
496 regions as we wanted to infer the overall point mutation rate in these regions.
497 Nucleotide dependent mutation rate estimates are shown in Supplementary
498 Figures 10 and 15. Nucleotide composition was adjusted for to calculate the
499 mutation rates of mutational signatures using standard tools⁴⁵.

500

501 **Data availability**

502 Sequencing data from healthy haematopoiesis is available from Lee-Six et al.¹³,
503 brain data during early development from Bae et al.¹², colorectal cancer data
504 from Cross et al.⁴⁰ and Roerink et al.⁴¹, renal cell carcinoma data from Gerlinger
505 et al.⁴² and lung carcinoma data from Jamal-Hanjani et al.⁴³.

506

507 **Acknowledgments**

508 A.S. is supported by the Wellcome Trust (202778/B/16/Z) and Cancer Research
509 UK (A22909). T.G. is supported by the Wellcome Trust (202778/Z/16/Z) and
510 Cancer Research UK (A19771). We acknowledge funding from the National
511 Institute of Health (NCI U54 CA217376) to A.S and T.A.G. This work was also
512 supported a Wellcome Trust award to the Centre for Evolution and Cancer
513 (105104/Z/14/Z). C.P.B. acknowledges funding from the Wellcome Trust
514 (209409/Z/17/Z).

515

516 **Author Contributions**

517 B.W. and A.S. conceived the study. B.W. and J.C. performed mathematical
518 analysis. B.W., M.J.W., K.C., D.T., J.F.M., G.D.C., D.N. W.C., I. S., W.H. & I.T.
519 contributed to data analysis and simulations. A.S. and T.A.G. supervised the
520 study. B.W., C.P.B., T.A.G. & A.S. wrote the manuscript. All authors read and
521 approved the manuscript.

522

523 **Competing Interests**

524 The authors declare no competing interests.

525

526 **Code availability**

527 The code for stochastic simulations of tumour growth is available at
528 <https://github.com/sottorivalab/CHESSE.cpp>. The code for the MCMC inference is
529 available at <https://github.com/sottorivalab/MCMC-MutationalDistances->.

530

531

532 **Figure Legends**

533

534 **Figure 1: Multi-region bulk sequencing encodes information on single cell lineages and**
535 **single cell divisions. a)** Each of the seven spatially separated tissue samples (in grey) consists of
536 thousands to millions of cells that descended from a single most recent common ancestor
537 (MRCA) cell. The genomic make-up of the single ancestral cell is described by the mutations
538 clonal to the bulk sample. Those appear at high variant allele frequency in the sample (bottom-
539 left panel, in purple). The intersection of mutations in any two bulk MRCA cells corresponds to
540 the genomic profile of another more ancestral cell. This process continues back in time until the
541 MRCA cell of all the sampled cells is reached. **b)** The level of genomic variation within a growing
542 tissue (e.g. development or cancer) is the direct consequence of mutation accumulation during
543 cell divisions, leading to a branching structure. Importantly, the most fundamental parameters,
544 the mutation rate μ and survival rate β of cells per division that drive this process are not directly
545 observable. **c)** Mutation rate per division μ and cell survival rate β leave identifiable fingerprints
546 in the observable patterns of genetic heterogeneity within a tissue. Cell divisions occur in
547 increments of natural numbers and thus the mutational distance between any two ancestral cells
548 is a multiple of the mutation rate μ .

549

550 **Figure 2: Distribution of mutational distances and computational validation. a)** The
551 quantized nature of cell divisions leads to a characteristic predicted distribution of mutational
552 distances across cell lineages. The shape of the distribution depends on the exact values of μ and
553 β . Roughly four different scenarios of combinations of small and large μ and β are possible. They
554 influence the shape of the distribution differently and thus constructing the distribution of
555 mutational distances allows disentangling the mutation rate μ and cell survival rate β . **b)** Spatial
556 stochastic simulations confirm the ability of mutational distance distributions to disentangle
557 mutation and lineage expansion rates (red area shows the spatial spread of a subclonal
558 mutation). Dots show mutational distances inferred from 200 samples of a single stochastic
559 computer simulation ($\mu = 20, \beta = 0.95$), the dashed line is the predicted distribution based on
560 our equation 7. **c)** A Monte Carlo Markov Chain inference framework based on mutational
561 distance distributions reliably identifies mutation and lineage expansion rates in simulations of
562 spatial and stochastically growing tissues (2 dimensional spatial stochastic simulations, μ :

563 Spearman $Rho = 0.98, p = 4 \times 10^{-23}$; β : Spearman $Rho = 0.93, p = 8 \times 10^{-16}$, Relative error:
564 $\eta_{\mu} = 0.056, \eta_{\beta} = 0.045$).

565

566 **Figure 3: Per-cell mutation and per-cell survival rate inferences in healthy haematopoiesis**

567 **during development. a)** Mutational distance distribution inferred from 89 whole genome
568 sequenced healthy haematopoietic stem cells from ref¹³ (black dots), and best theoretical fit
569 (grey line). Posterior parameter distribution of the MCMC inference for **b)** the mutation rate per
570 cell division ($\mu L = 1.14_{-0.24}^{+0.12}$ mutations per genome per cell division) and **c)** the cell survival rate
571 ($\beta = 0.96_{-0.102}^{+0.038}$). Median point estimates and 95% credibility intervals were taken from the
572 posterior parameter distributions. The inferred mutation rate per cell division agrees with the
573 original estimation of 1.2 mutations per cell division. Furthermore, our joined inference of
574 mutation and cell survival rate confirms the original assumption of no cell death during early
575 development of haematopoiesis.

576

577 **Figure 4: Per-cell mutation and per-cell survival rate inferences in single neurons during**

578 **development a)** Mutational distance distribution inferred from 14 whole genome sequenced
579 single neurons from ref¹² derived from one fetus (17w4d past conception) (black dots), and best
580 theoretical fit (grey line). MCMC inference for **b)** the mutation rate per cell division ($\mu L =$
581 $1.37_{-0.1}^{+0.1}$ mutations per genome per cell division) and **c)** the per-cell survival rate ($\beta =$
582 $0.998_{-0.01}^{+0.002}$). Median point estimates and 95% credibility intervals were taken from the posterior
583 parameter distributions. The inferred mutation rate per cell division agrees with the original
584 estimation of 1.3 mutations per cell division. Furthermore, our joined inference of mutation and
585 cell survival rate confirms the original assumption of no cell death during early brain
586 development.

587

588 **Figure 5: Mutational distance for three colorectal tumours. a-c)** Examples of the mutational

589 distance distribution on single chromosomes for three different colorectal carcinomas for which
590 6, 7 and 9 multi-region bulk samples were sequenced at whole-genome resolution (dots=data,
591 dashed line=theoretical prediction based on MCMC parameter estimates – see insets). The
592 distribution of mutational distances differs between patients, with Patient 04 (MSI –
593 Microsatellite Instability) showing one order of magnitude larger mutational distances. **d-f)** Per-
594 cell mutation rate per chromosome separated by trinucleotide mutational signature. Results are
595 consistent across chromosomes, as expected (Methods). **g-i)** The mean overall mutation rates are
596 ($\mu_{02} = (1.0_{-0.07}^{+0.46}) \times 10^{-8}, \mu_{03} = (2.4_{-0.19}^{+0.41}) \times 10^{-8}$ and $\mu_{04} = (3.1_{-0.12}^{+0.35}) \times 10^{-8}$ bp/division
597 dashed lines), 20 to 60 times higher compared to healthy somatic cells. Patient 04 is MSI+
598 highlighted by signature 6. **j-l)** Estimates of per-cell survival rates per chromosome are
599 consistent across chromosomes of the same patient (Median:
600 $\beta_{02} = 0.51_{-0.05}^{+0.05}, \beta_{03} = 0.65_{-0.02}^{+0.02}, \beta_{04} = 0.34_{-0.01}^{+0.01}$), but vary considerably between patients
601 (Supplementary Figure 12).

602

603 **Figure 6: Map of per-cell mutation and per-cell survival rates across cancer types.** For each

604 of the 16 tumours analysed we plot the per-cell mutation rate versus the per-cell survival rate.

605 Median estimates and 95% credibility intervals for the mutation and cell survival rate are

606 derived from the MCMC inferences as described in the main text. Dashed lines correspond to

607 values of healthy tissue ($\mu_h = 1 \times 10^{-9}$, $\beta_h = 1/3$). White background corresponds to β values608 that allow for growing cell populations as $\beta = 1/3$ corresponds to stable (homeostatic)609 populations. Shaded area describes values of β that would lead to population extinction. Most

610 cancers scatter across the map, indicating extensive inter-patient heterogeneity.

611

612

613

614

615

Tissue type	Sequencing	# Samples	μ $\times 10^{-9}$	β	Source
HSC (development)	Whole Genome	89	0.39	0.96	Lee-Six
Neuron (development)	Whole Genome	14	0.46	0.99	Bae
CRA	Exome	6	2.91	0.46	Cross
CRC (MSS)	Exome	13	30.1	0.84	Cross
CRC (MSS)	Exome	8	12.5	0.43	Cross
CRC (MSS)	Whole Genome	6	24.0	0.65	Cross
CRC (MSS)	Whole Genome	7	10	0.51	Cross
CRC (MSS)	Whole Genome	9	8.9	0.45	Roerink
CRC (MSS)	Whole Genome	9	9.9	0.50	Roerink
CRC (MSI)	Whole Genome	9	30.9	0.34	Cross
CRC (MSI)	Whole Genome	7	17.9	0.47	Roerink
CCRCC	Exome	8	21.7	0.66	Gerlinger
CCRCC	Exome	11	31.2	0.86	Gerlinger
CCRCC	Exome	8	15.8	0.47	Gerlinger
CCRCC	Exome	8	2.3	0.80	Gerlinger
CCRCC	Exome	8	2.1	0.72	Gerlinger
NSCLC	Exome	7	53	0.36	Jamal-Hanjani
NACLC	Exome	7	14	0.59	Jamal-Hanjani

616

617 **Table 1: Data summary and evolutionary parameter inferences.** The data of healthy tissue618 during development was taken from Lee-Six et al¹³ and Bae et al¹². Data on colorectal cancers is619 from Cross et al⁴⁰ and Roerink et al⁴¹, data on renal cell carcinoma from Gerlinger et al⁴² and data

620 on lung carcinomas from Jamal-Hanjani et al⁴³. Estimates for mutation and cell survival rates are
621 from best MCMC fits based on the distribution of mutational distances.

622

623

624 **References**

625

- 626 1. Sun, J. *et al.* Clonal dynamics of native haematopoiesis. *Nature* **514**,
627 322–327 (2014).
- 628 2. Busch, K. *et al.* Fundamental properties of unperturbed
629 haematopoiesis from stem cells in vivo. *Nature* **518**, 542–546 (2015).
- 630 3. Frank, S. A. Somatic evolutionary genomics: Mutations during
631 development cause highly variable genetic mosaicism with risk of
632 cancer and neurodegeneration. *Proceedings of the National Academy*
633 *of Sciences* **107**, 1725–1730 (2010).
- 634 4. Nowell, P. The Clonal Evolution of Tumor Cell Populations. *Science*
635 **194**, 23–28 (1976).
- 636 5. Greaves, M. & Maley, C. C. Clonal evolution in cancer. *Nature* **481**,
637 306–313 (2012).
- 638 6. Swanton, C. Intratumor Heterogeneity: Evolution through Space and
639 Time. *Cancer Research* **72**, 4875–4882 (2012).
- 640 7. McGranahan, N. & Swanton, C. Clonal Heterogeneity and Tumor
641 Evolution: Past, Present, and the Future. *Cell* **168**, 613–628 (2017).
- 642 8. McGranahan, N. & Swanton, C. Biological and Therapeutic Impact of
643 Intratumor Heterogeneity in Cancer Evolution. *Cancer Cell* **27**, 15–26
644 (2015).
- 645 9. Khan, K. H. *et al.* Longitudinal Liquid Biopsy and Mathematical
646 Modeling of Clonal Evolution Forecast Time to Treatment Failure in
647 the PROSPECT-C Phase II Colorectal Cancer Clinical Trial. *Cancer*
648 *Discov* (2018).
- 649 10. Martincorena, I. *et al.* High burden and pervasive positive selection of
650 somatic mutations in normal human skin. *Science* **348**, 880–886
651 (2015).
- 652 11. Martincorena, I. *et al.* Somatic mutant clones colonize the human
653 esophagus with age. *Science* **57**, eaau3879 (2018).
- 654 12. Bae, T. *et al.* Different mutational rates and mechanisms in human
655 cells at pregastrulation and neurogenesis. *Science* **543**, eaan8690
656 (2017).
- 657 13. Lee-Six, H. *et al.* Population dynamics of normal human blood
658 inferred from somatic mutations. *Nature* **561**, 473–478 (2018).
- 659 14. Werner, B. & Sottoriva, A. Variation of mutational burden in healthy
660 human tissues suggests non-random strand segregation and allows
661 measuring somatic mutation rates. *PLoS Comput Biol* **14**, e1006233

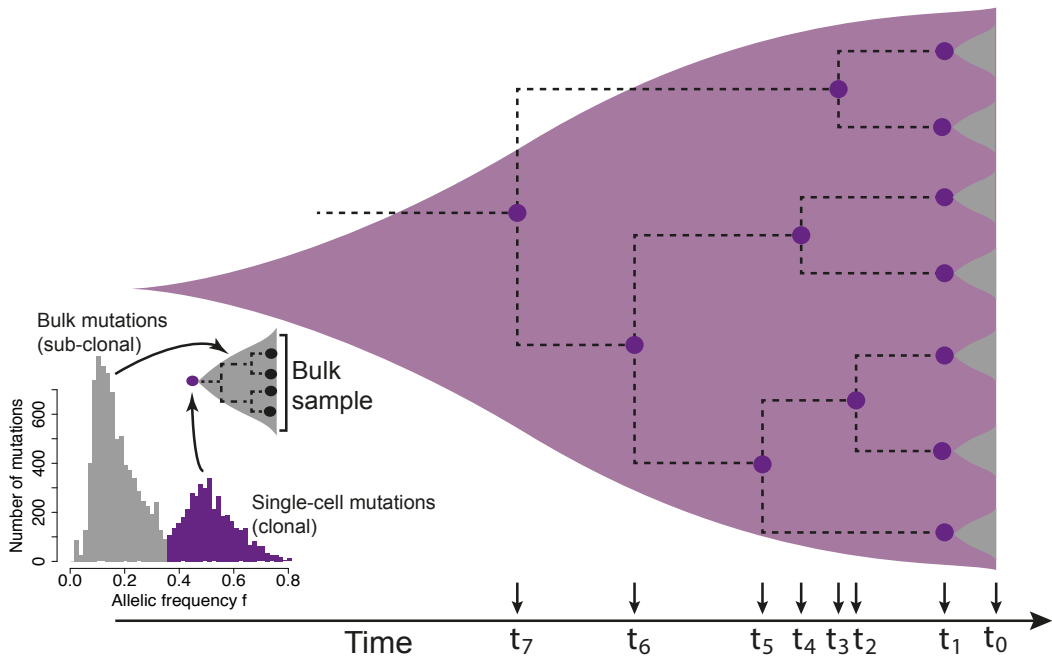
- 662 (2018).
- 663 15. Burrell, R. A., McGranahan, N., Bartek, J. & Swanton, C. The causes and
664 consequences of genetic heterogeneity in cancer evolution. *Nature*
665 **501**, 338–345 (2013).
- 666 16. Lynch, M. Evolution of the mutation rate. *Trends in Genetics* **26**, 345–
667 352 (2010).
- 668 17. Lynch, M. *et al.* Genetic drift, selection and the evolution of the
669 mutation rate. *Nature Reviews Genetics* **17**, 704–714 (2016).
- 670 18. Williams, M. J., Werner, B., Barnes, C. P., Graham, T. A. & Sottoriva, A.
671 Identification of neutral tumor evolution across cancer types. *Nature*
672 *Genetics* **48**, 238–244 (2016).
- 673 19. Williams, M. J. *et al.* Quantification of subclonal selection in cancer
674 from bulk sequencing data. *Nature Genetics* **50**, 895–903 (2018).
- 675 20. Slatkin, M. & Hudson, R. R. Pairwise Comparisons of Mitochondrial
676 DNA Sequences in Stable and Exponentially Growing Population.
677 *Genetics* **129**, 555–562 (1991).
- 678 21. Donnelly, P. & Tavaré, S. Coalescence and Genealogical Structure under
679 Neutrality. *Annual Reviews of Genetics* **29**, 401–421 (1995).
- 680 22. Stadler, T. *et al.* How well can the exponential-growth coalescent
681 approximate constant-rate birth–death population dynamics?
682 *Proceedings of the Royal Society B: Biological Sciences* **282**, 20150420
683 (2015).
- 684 23. Chkhaidze, K. *et al.* Spatially constrained tumour growth affects the
685 patterns of clonal selection and neutral drift in cancer genomic data.
686 *PLoS Comput Biol* **15**, e1007243 (2019).
- 687 24. Gillespie, D. T. A general method for numerically simulating the
688 stochastic time evolution of coupled chemical reactions. *Journal of*
689 *Computational Physics* **22**, 403–434 (1976).
- 690 25. Werner, B. *et al.* Reconstructing the *in vivo* dynamics of
691 hematopoietic stem cells from telomere length distributions. *eLife*
692 **10.7554**, e08687v2 (2015).
- 693 26. Rahbari, R. *et al.* Timing, rates and spectra of human germline
694 mutation. *Nature Genetics* **48**, 126–133 (2015).
- 695 27. Blokzijl, F. *et al.* Tissue-specific mutation accumulation in human
696 adult stem cells during life. *Nature* **538**, 260–264 (2016).
- 697 28. Lodato, M. A. *et al.* Aging and neurodegeneration are associated with
698 increased mutations in single human neurons. *Science* **359**, 555–559
699 (2018).
- 700 29. Milholland, B. *et al.* Differences between germline and somatic
701 mutation rates in humans and mice. *Nature Communications* **8**, 1–8
702 (2017).
- 703 30. Brody, Y. *et al.* Quantification of somatic mutation flow across
704 individual cell division events by lineage sequencing. *Genome Res.* **28**,
705 1901–1918 (2018).
- 706 31. Alexandrov, L. B. *et al.* Clock-like mutational processes in human
707 somatic cells. *Nature Genetics* **47**, 1402–1407 (2015).
- 708 32. Bozic, I. *et al.* Accumulation of driver and passenger mutations during
709 tumor progression. *Proceedings of the National Academy of Science*
710 **107**, 18545–18550 (2010).

- 711 33. Bozic, I., Gerold, J. M. & Nowak, M. A. Quantifying Clonal and
712 Subclonal Passenger Mutations in Cancer Evolution. *PLoS Comput*
713 *Biol* **12**, e1004731 (2016).
- 714 34. Gerstung, M. *et al.* The evolutionary history of 2,658 cancers. *BioRxiv*
715 (2017). doi:10.1101/312041
- 716 35. Rubanova, Y. *et al.* TrackSig: reconstructing evolutionary trajectories
717 of mutations in cancer. *BioRxiv* **49**, 1015 (2018).
718 doi:10.1101/260471
- 719 36. Chen, X. *et al.* Single-cell analysis at the threshold. *Nature*
720 *Biotechnology* **34**, 1111–1118 (2016).
- 721 37. Davis, A. & Navin, N. E. Computing tumor trees from single cells.
722 *Genome Biology* 1–4 (2016). doi:10.1186/s13059-016-0987-z
- 723 38. Diaz, L. A. *et al.* The molecular evolution of acquired resistance to
724 targeted EGFR blockade in colorectal cancers. *Nature* **486**, 537–540
725 (2012).
- 726 39. Lipinski, K. A. *et al.* Cancer Evolution and the Limits of Predictability
727 in Precision Cancer Medicine. *TRENDS in CANCER* **2**, 49–63 (2016).
- 728 40. Cross, W. *et al.* The evolutionary landscape of colorectal
729 tumorigenesis. *Nature Ecology & Evolution* 1–14 (2018).
- 730 41. Roerink, S. F. *et al.* Intra-tumour diversification in colorectal cancer at
731 the single-cell level. *Nature* **556**, 457–462 (2018).
- 732 42. Gerlinger, M. *et al.* Genomic architecture and evolution of clear cell
733 renal cell carcinomas defined by multiregion sequencing. *Nature*
734 *Genetics* **46**, 225–233 (2014).
- 735 43. Jamal-Hanjani, M. *et al.* Tracking the Evolution of Non–Small-Cell
736 Lung Cancer. *New England Journal of Medicine* **376**, 2109–2121
737 (2017).
- 738 44. Temko, D., Tomlinson, I. P. M., Severini, S., Schuster-Böckler, B. &
739 Graham, T. A. The effects of mutational processes and selection on
740 driver mutations across cancer types. *Nature Communications* 1–10
741 (2018).
- 742 45. Gehring, J. S., Fischer, B., Lawrence, M. & Huber, W.
743 SomaticSignatures: inferring mutational signatures from single-
744 nucleotide variants. *Bioinformatics* **31**, 3673–3675 (2015).
745
746
747
748
749
750
751
752
753
754
755
756
757
758
759

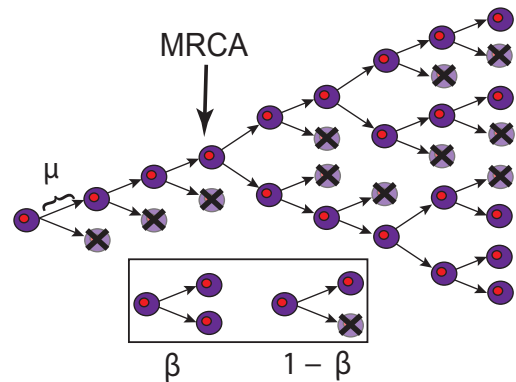
760
761
762
763
764

a) Multi-region bulk sequencing

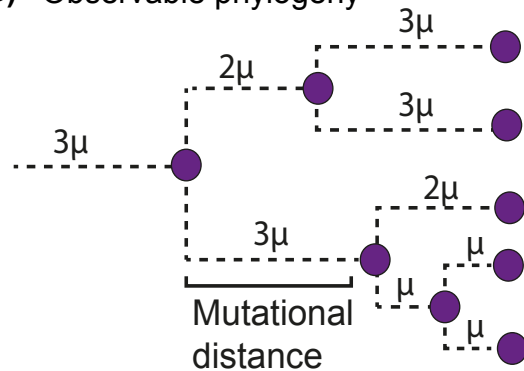
● Single cells
 ●-----● Single lineages
 MRCA \rightarrow ● Bulk sample

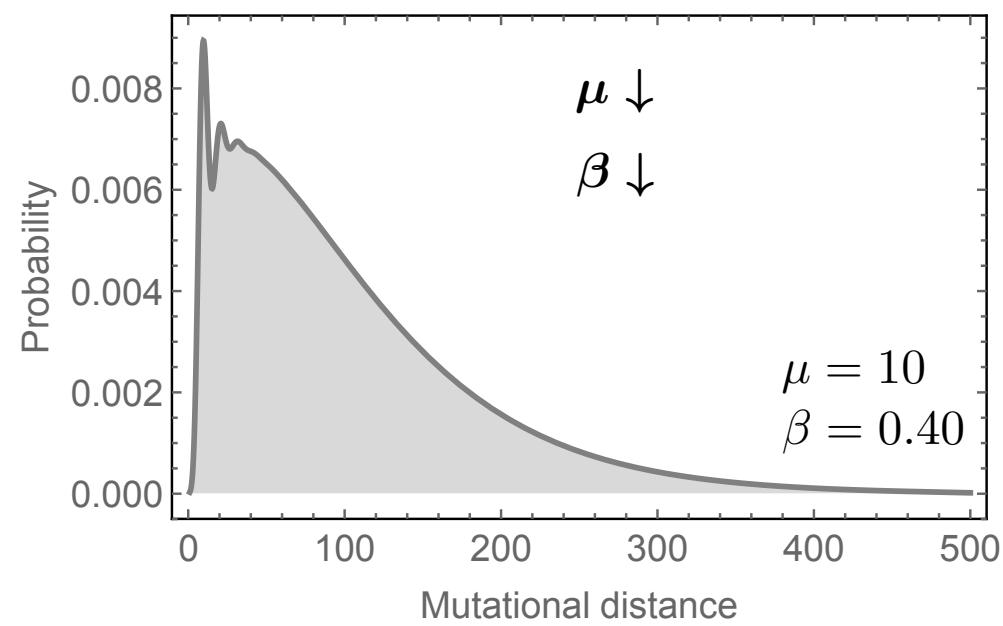
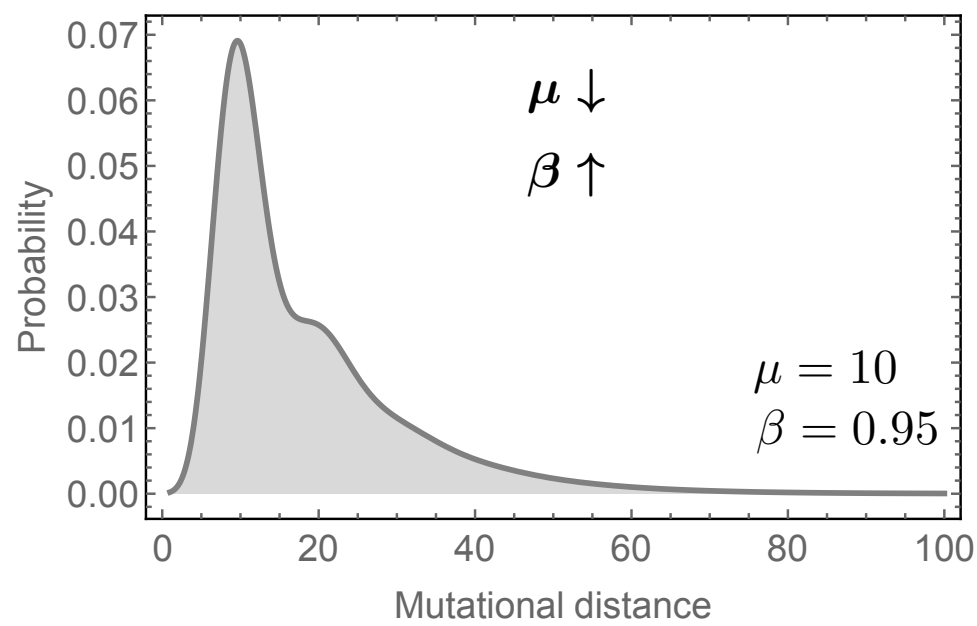
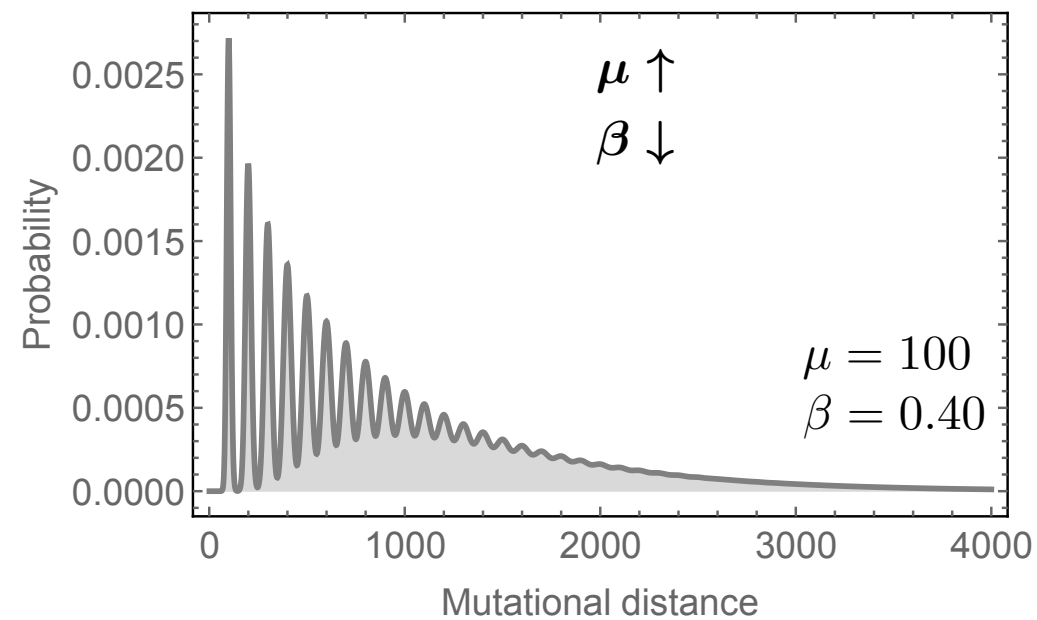
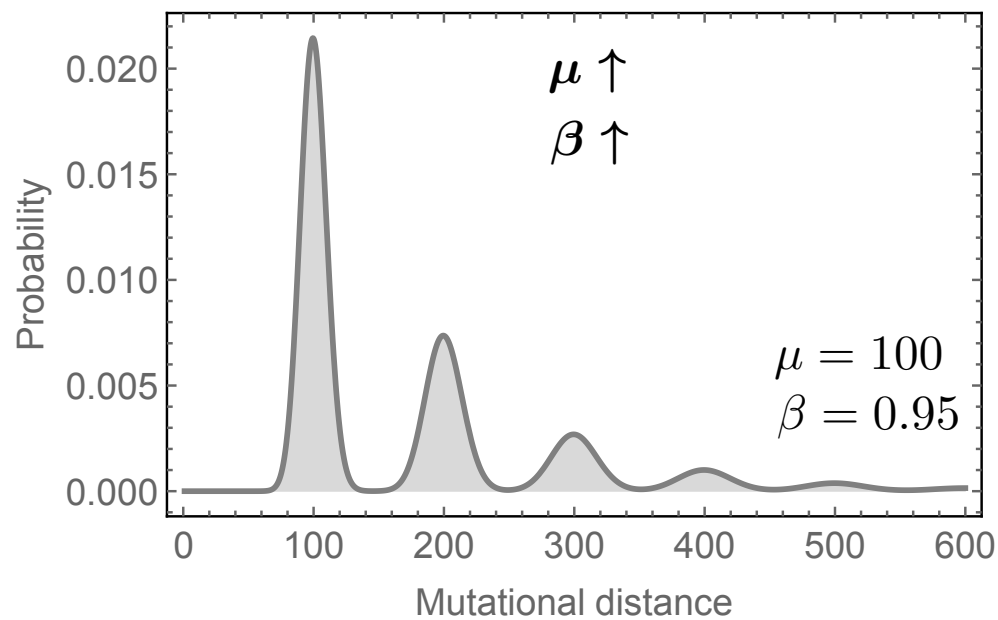
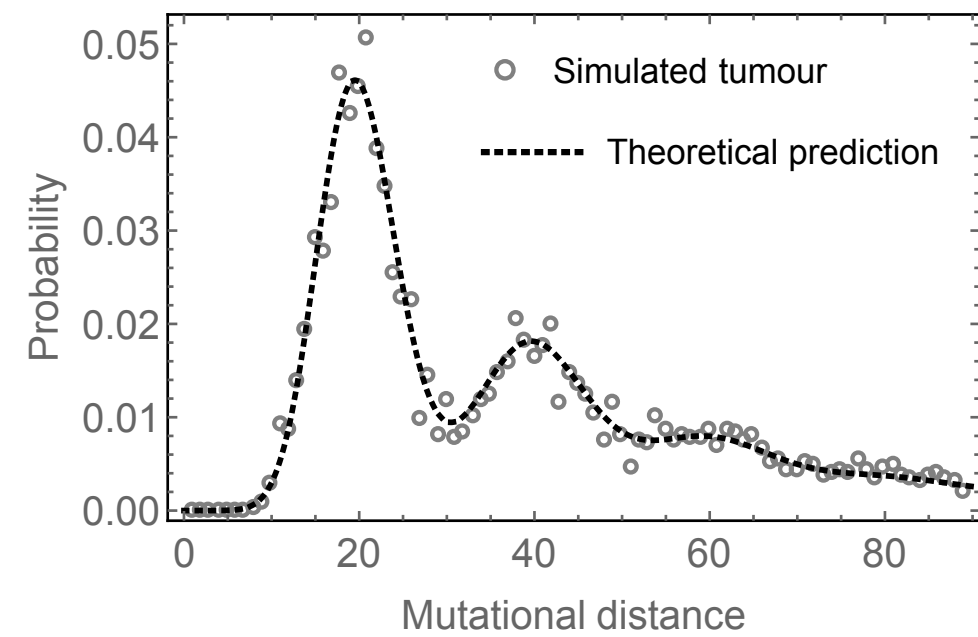
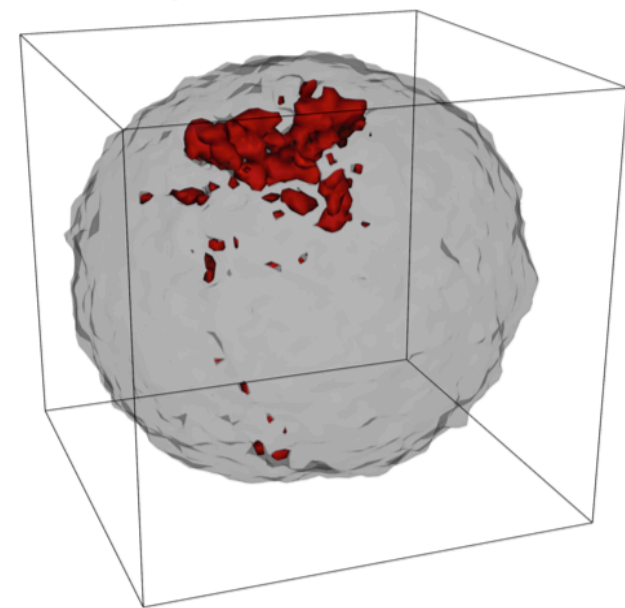
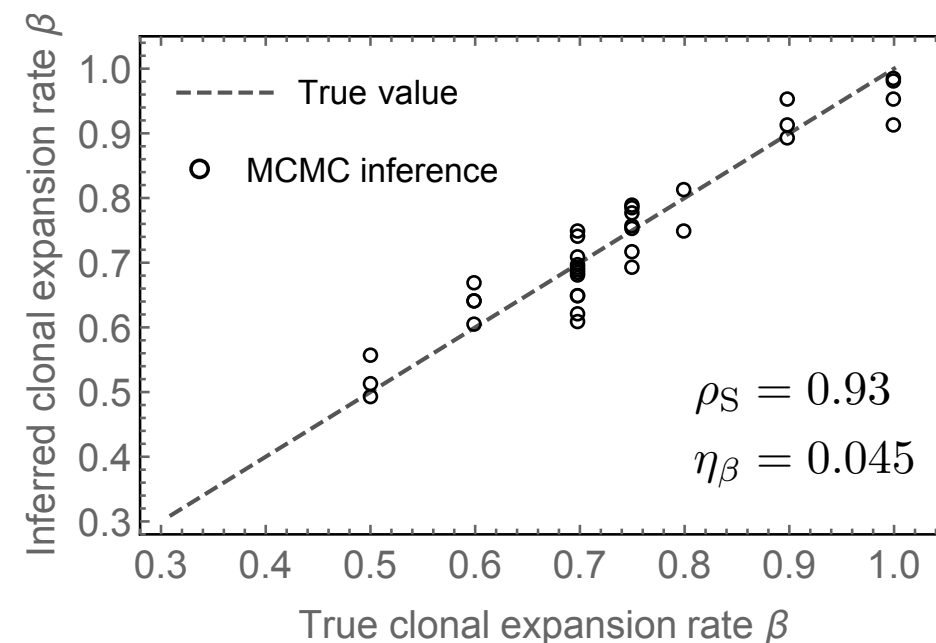
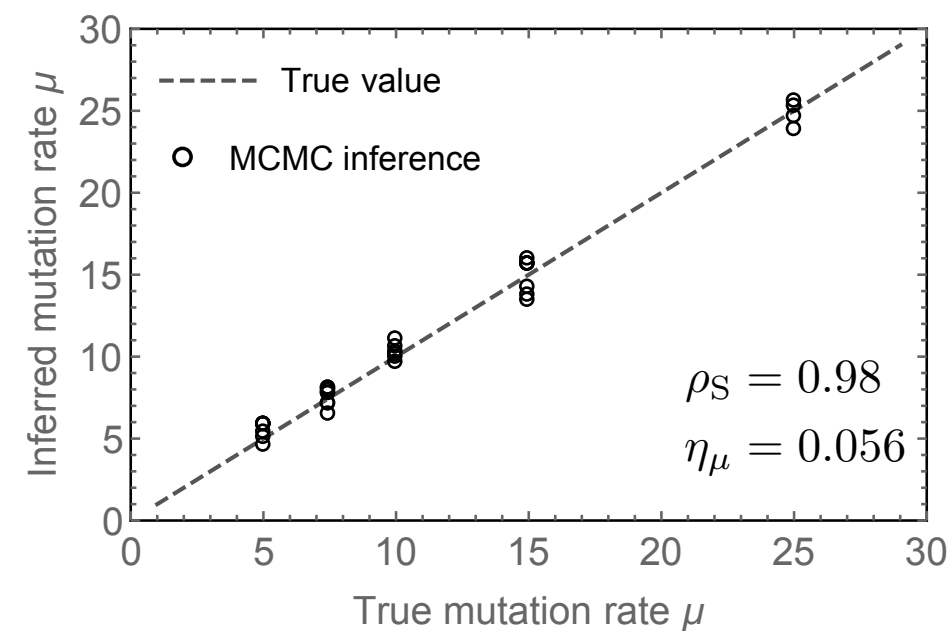


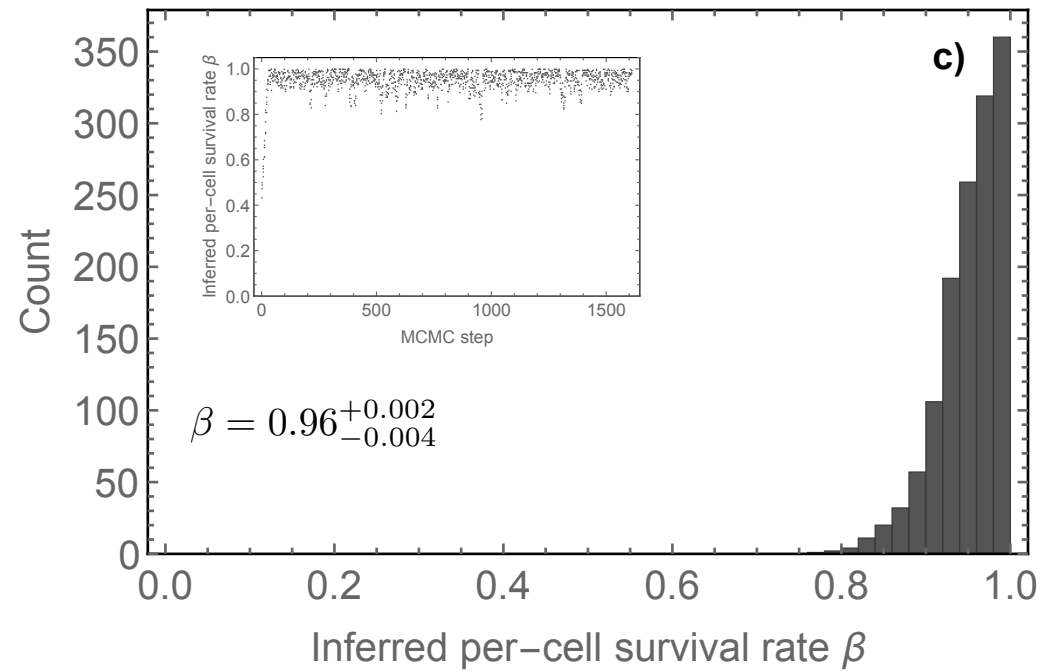
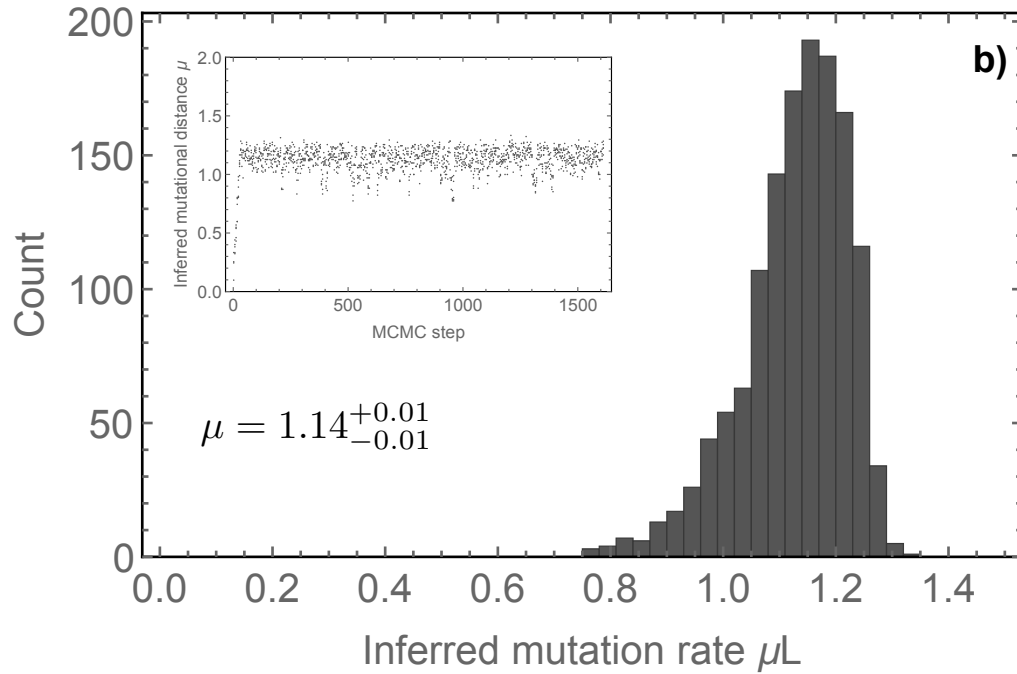
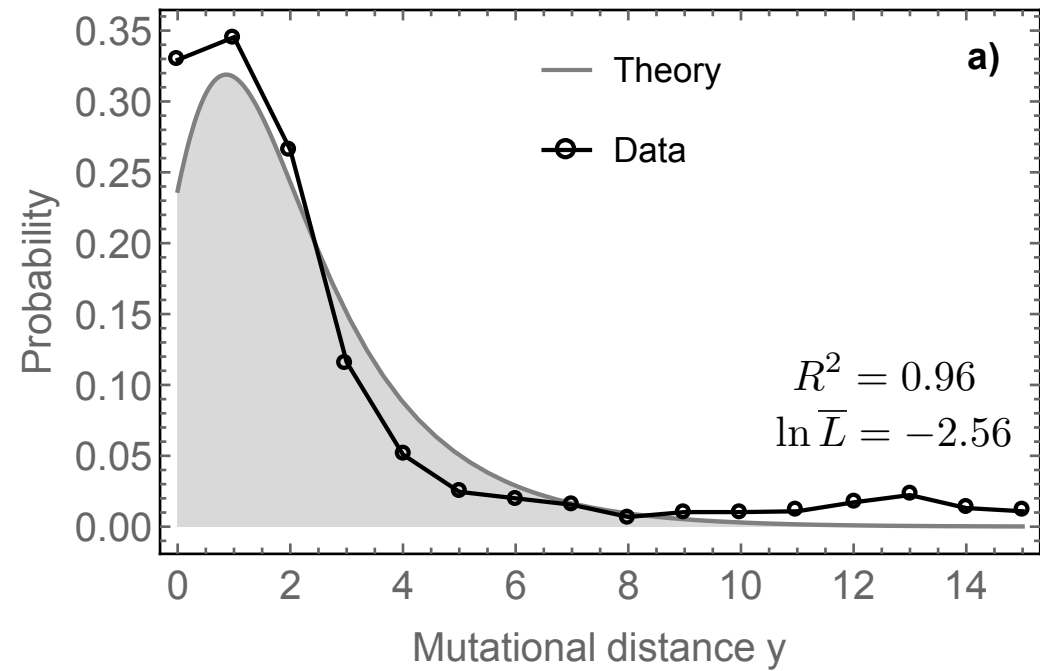
b) Unobservable cell dynamics

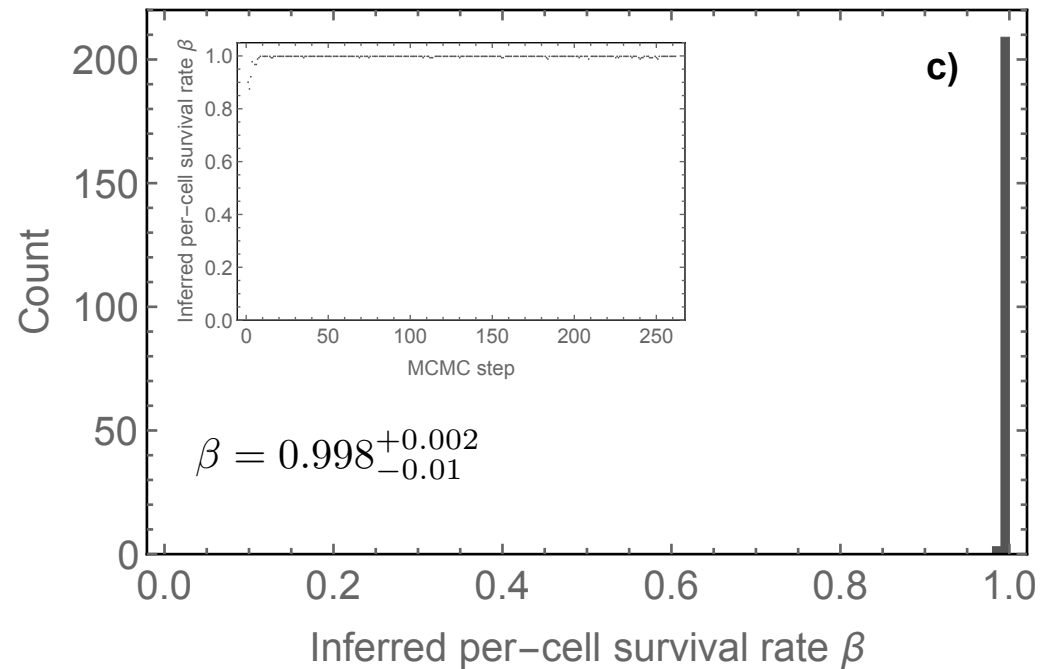
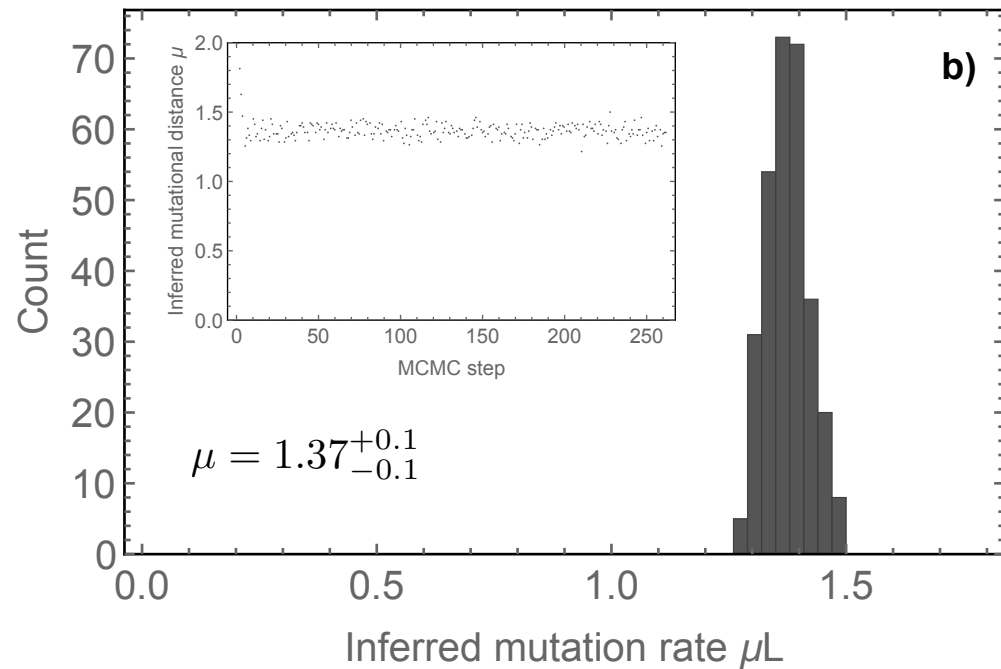
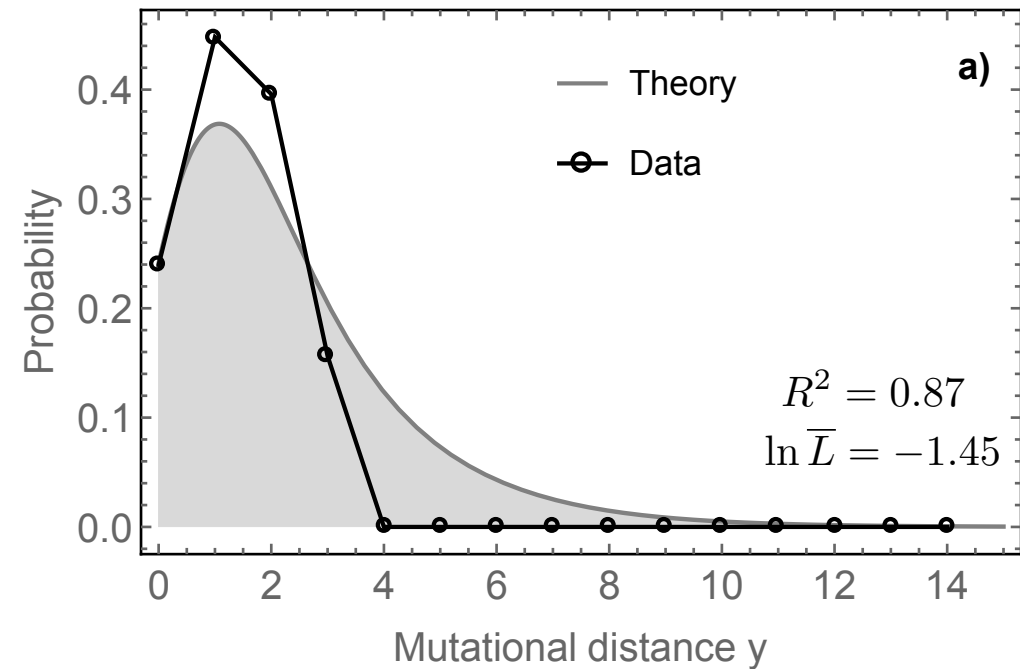


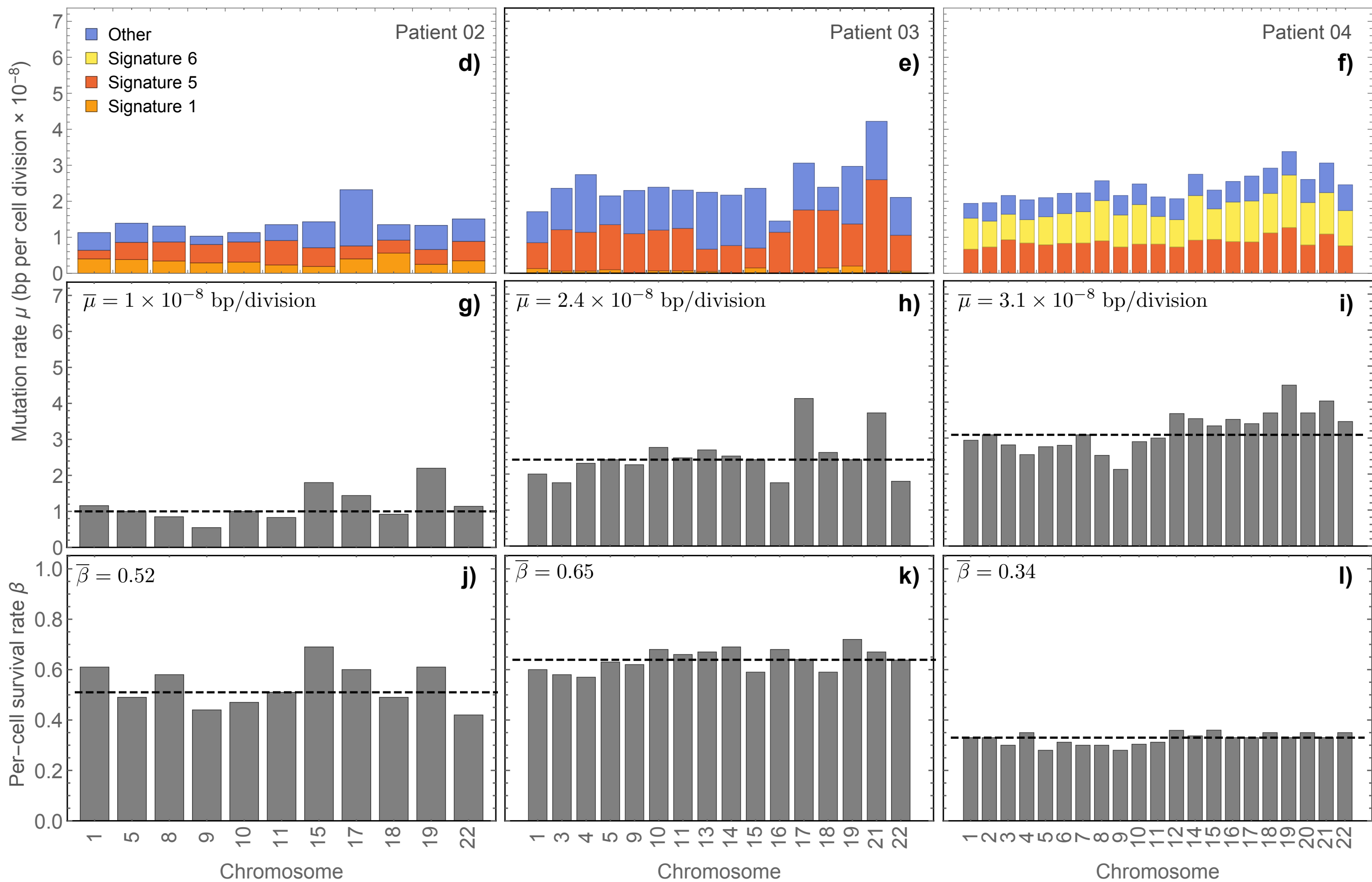
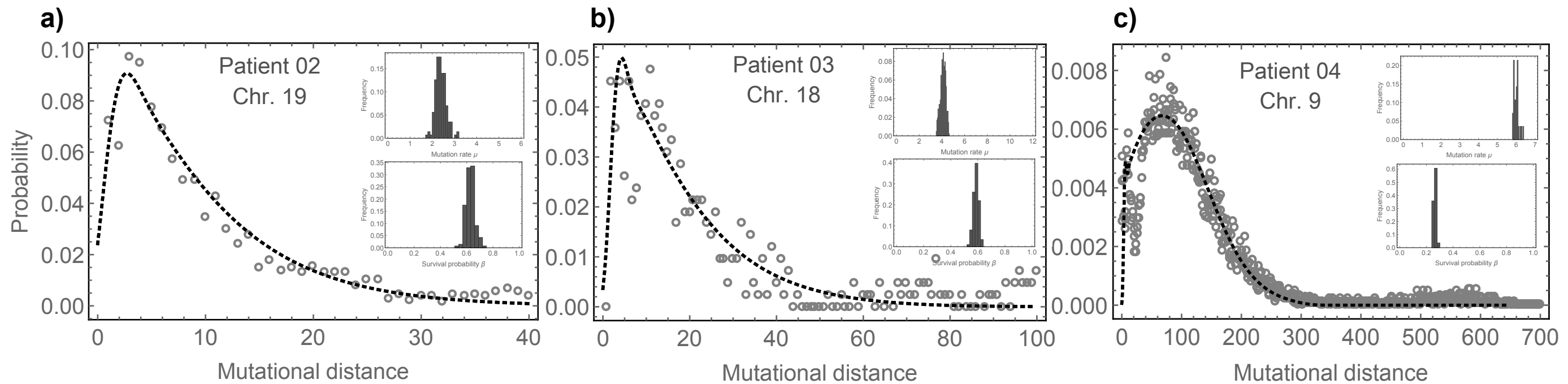
c) Observable phylogeny



a) Distribution of mutational distances**b) Computational validation****c) MCMC parameter inference**







- Colon Adenoma (CRA)
- Colon Carcinoma (MSI) (CRC)
- Colon Carcinoma (MSS) (CRC)
- Renal Cell Carcinoma (CCRCC)
- Lung Squamous Cell Carcinoma (NSCLC)
- Lung Adenosquamous Carcinoma (NSCLC)
- Healthy Tissue

